# A Multi-Sensor Tactile System Based on Fiber Bragg Grating Sensors for Soft Tissue Palpation

M. Pulcinelli⬛, *Graduate Student Member, IEEE*, L. Zoboli,
F. De Tommasi⬛, *Graduate Student Member, IEEE*, C. Massaroni⬛, *Senior Member, IEEE*,
V. Altomare, A. Grasso, A. Gizzi⬛, *Senior Member, IEEE*, E. Schena⬛, *Senior Member, IEEE*,
and D. Lo Presti⬛, *Member, IEEE*

**Abstract**—**Superficial tissue palpation is a clinical examination to detect tumors in soft tissue, like breast, by applying variable forces on its surface. Recently, instrumented tactile probes based on different technologies (e.g., electrical and optical sensors) were developed to quantitatively detect changes in tissue stiffness, improving the chances of early tumor diagnosis. Among many options to develop tactile probes, fiber Bragg grating (FBG) sensors are gaining increasing traction, thanks to their superior potentials (e.g., high sensitivity, small dimensions, electromagnetic immunity interferences, and multiplexing capability). This study proposed a multi-FBG sensors tactile system for superficial breast palpation, as an optimization of a previously designed prototype, in terms of dimensions and number of sensors.**



**It represents the first step toward the creation of a matrix of sensors for optimizing tumor identification. In detail, a three-FBG array was integrated into a 3-D-printed structure to simultaneously investigate multiple measurement sites, enhance the system's spatial resolution, and minimize the probe encumbrance. The design of the system was guided by a finite element analysis (FEA). Then, a metrological characterization was performed, focusing on the investigation of the FBGs sensitivity to force and analysis of the crosstalk effects among sensors within the same structure. Subsequently, palpation tests on phantoms mimicking soft tissues with a tumor were conducted, revealing the ability of the fabricated system to detect stiffer materials within flexible substrates. These findings make the proposed system an ideal candidate for diagnostic tissue palpation.**

**Index Terms**—**3-D printing, breast cancer detection, fiber Bragg gratings (FBGs), tactile sensor, tissue palpation.**
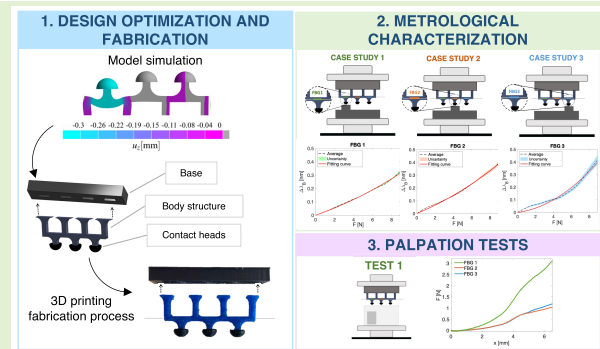
## I. INTRODUCTION

**D**IAGNOSTIC tissue palpation represents one of the most common preliminary examinations for detecting tumor

M. Pulcinelli, F. De Tommasi, C. Massaroni, E. Schena, and D. Lo Presti are with the Unit of Measurements and Biomedical Instrumentation, Università Campus Bio-Medico di Roma (UCBM), 00128 Rome, Italy (e-mail: d.lopresti@unicampus.it).
L. Zoboli and A. Gizzi are with the Unit of Nonlinear Physics and Mathematical Models, Università Campus Bio-Medico di Roma (UCBM), 00128 Rome, Italy (e-mail: l.zoboli@unicampus.it; a.gizzi@unicampus.it).
V. Altomare and A. Grasso are with the Breast Surgery Unit, Fondazione Policlinico Universitario Campus Bio-Medico, 00128 Rome, Italy (e-mail: v.altomare@policlinicocampus.it; a.grasso@policlinicocampus.it).

masses in soft tissue, like breast tissue. Identifying any tissue alterations at the earliest possible stage is crucial for ensuring optimal treatment choices and enhancing the patient survival and recovery rate [1]. Diagnostic tissue palpation falls into two primary categories: invasive palpation (employed during minimally invasive surgery, MIS) and noninvasive one (i.e., superficial palpation [2], [3]). The superficial palpation consists of applying a varying force ($F$) on the tissue to identify any lumps or tumor masses, characterized by greater stiffness compared to healthy tissue [4]. This examination serves as a preventive tool for tracking any tissue alterations over time, before proceeding with more accurate diagnostic methods (e.g., mammography, magnetic resonance imaging, and ultrasound screening) [5], [6]. Despite its significant potential, the reliability of superficial palpation examinations still heavily relies on the experience and attention of the examiner [7], [8], [9], [10]. Hence, the utilization of tactile probes to quantitatively evaluate alterations in tissue stiffness plays a pivotal role in improving tumor identification at its early stage [7]. So far, various innovative solutions based

on different technologies, such as capacitive, piezoresistive, piezoelectric, and fiber Bragg grating (FBG) sensors have been proposed [2], [11], [12], [13], [14], [15], [16], [17]. Among these, FBG-based solutions are gaining increasing traction thanks to their superior potentials that exceed the limits of electrical technologies (e.g., limited $F$ sensitivity, high power consumption, sterilization problems, and the necessity for numerous output cables) [7], [15], [18], [19]. FBGs show benefits in terms of high sensitivity, spatial resolution, electromagnetic interference immunity, and multiplexing capabilities (i.e., multiple FBGs can be inscribed into the same optical fiber). All these benefits promote FBG integration into miniaturized tools [20], [21]. To date, FBGs are widely used to sensorize devices for invasive tissue palpation during MIS procedures [15], [19], while their utilization for superficial tissue investigation is still limited.

To date, to the best of the authors' knowledge, only one 3-D-printed tactile probe based on FBG technology with its subsequent design optimization was proposed for superficial tissue characteristics investigation [11], [22]. This probe was designed to apply varying $F$ values to the breast surface to identify lesions within the tissue. This system integrated three sensing units with the same shape, each encapsulating a single 10 mm long FBG. However, the consequence of the big size of the units is low spatial resolution; in addition, this limits the number of sensors to integrate into the probe and, in turn, its performance in tumor detection [11], [22]. In contrast, an instrumented tool for diagnostic palpation examinations should exhibit high spatial resolution to detect smaller lesions in their early stages, enhancing the likelihood of a prompt cancer diagnosis. A method to increase the spatial resolution is to exploit a multi-sensor approach based on array configurations for designing the sensing units with a reduced encumbrance.

A potential solution consists of integrating multiple sensors (e.g., FBGs) within the same sensing structure. This can lead to a more compact and miniaturized tactile system that allows the simultaneous investigation of small regions of tissue.

In this work, we proposed a multi-sensor approach by integrating an array of three FBGs into a 3-D-printed structure with small dimensions capable of providing a significant boost to the field of breast palpation. In particular, a further optimization of the sensing unit of the tactile probe already described in [11] was carried out.

Our focus was on enhancing the spatial resolution of the tactile sensing structure by increasing the number of sensors and reducing its overall size to investigate multiple measurement sites simultaneously. To achieve these goals, two key achievements were pursued: 1) a reduction in dimensions of the sensing unit of ~50% of its original structure [11] and 2) an increase in the number of sensors integrated into the same 3-D-printed structure. These optimizations mark relevant improvements in the system properties such as high spatial resolution, reduced size, and limited incumbrance.

The remainder of the work is organized as follows. In Section II, the working principle of the tactile sensing structure is described. Section III outlines the finite element analysis (FEA) that guided the design optimization and the manufacturing process of the system. Section IV detailed the metrological characterization of the proposed system in terms of sensitivity to $F$ and the crosstalk among the multiple FBGs enclosed within the same structure. Finally, Section V describes the fabrication process of different silicone phantoms with a rigid block inside to mimic breast tissues with tumors, and the results of compression tests conducted to assess the ability of the embedded FBGs to work simultaneously in the detection of tumors.

## II. MULTI-SENSOR TACTILE SYSTEM BASED ON FBG TECHNOLOGY: BACKGROUND AND WORKING PRINCIPLE

An FBG is a specific type of fiber optic sensor. It is manufactured by exposing a portion of the core of a single-mode optical fiber to an intense UV laser light, thus resulting in a permanent period perturbation of the refractive index of the fiber core. An FBG works as a bandpass filter: when a broadband spectrum of light signal passes through the fiber, the FBG reflects a narrow range of wavelengths centered around the so-called Bragg wavelength ($\lambda_B$). The $\lambda_B$ value depends on the effective refractive index of the fiber core, $n_{eff}$ and the grating period, $\Lambda$ according to the following relationship [23]:

$$\lambda_B = 2 \cdot n_{eff} \cdot \Lambda. \tag{1}$$

When an FBG is subjected to strain ($\varepsilon$) or temperature variations ($\Delta T$), the $\lambda_B$ experiences a shift ($\Delta\lambda_B$) due to a modification of $n_{eff}$ and $\Lambda$. This phenomenon follows a linear relationship, where the $\Delta\lambda_B$ is directly proportional to the applied $\varepsilon$ and $\Delta T$:

$$\frac{\Delta\lambda_B}{\lambda_B} = (1 - \rho_e) \cdot \varepsilon + (\alpha + \xi) \cdot \Delta T \tag{2}$$

where $\rho_e$, $\alpha$, and $\xi$ represent the effective photoelastic, thermal expansion, and thermo-optic coefficient, respectively.

When encapsulated into an external substrate, an FBG can also exhibit sensitivity to other parameters, like $F$ and relative humidity (RH) [23], [24], [25], [26], [27], [28], [29]. Particularly, when integrated into specifically designed structures, the FBG output can be influenced by the properties of the materials used for its encapsulation [30], [31], [32].

In this work, we proposed a multi-sensor system to transduce $F$ into $\varepsilon$ along the longitudinal axis of the fiber during superficial breast palpation applications. The system is composed of three main parts: 1) a 3-D-printed body structure to enclose a three-FBG array; 2) three contact heads to better transmit the applied $F$ to the body structure; and 3) a base to fit the flanges of the body structure for its stable integration into the probe in [11].

In a real application scenario, the developed system is expected to work as follows: when the contact heads are pushed against a soft tissue, the portions of the body structure under the heads experience a flexion, inducing a deformation on the three FBGs, which means an increase in their $\Delta\lambda_B$ values. However, when one of the contact heads encounters a more rigid material (e.g., a tumor) than the surrounding
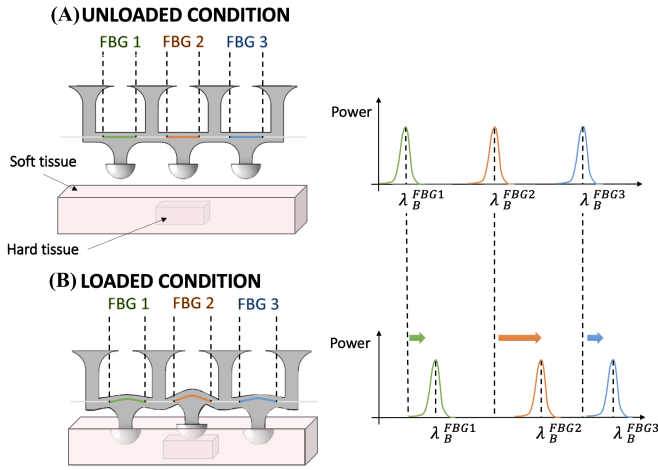
Fig. 1. Working principle of the FBG array embedded in the 3-D-printed body structure when a harder tissue (e.g., tumor mass) is located under the central contact head of the multi-sensor tactile system. (A) Output of the FBG array before the central contact head encounters the harder tissue. (B) Output of the FBG array when the central contact head pushes on the surface of the harder tissue.
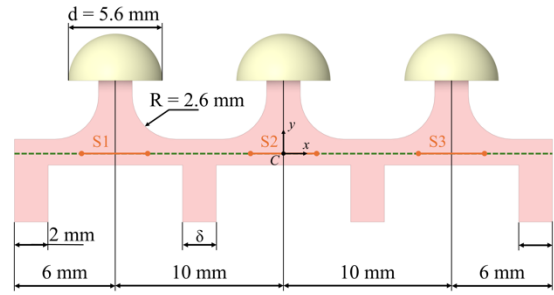


Fig. 2. Design and dimensions of the multi-sensor tactile system. The dotted green line represents the position of the optical fiber, while the orange segments S1, S2, and S3 are the location of the FBGs.

TABLE I
WIDTH OF THE INTERMEDIATE COLUMNS IN THE
MULTI-SENSOR TACTILE SYSTEM

|  | 2-flanges | 4-flanges | 6-flanges |
|---|---|---|---|
| $\delta$ [mm] | 0 | 2 | 4 |

tissue, the FBG located exactly under the contact head pressed against the stiffer mass experiences a major increase in the $\Delta\lambda_B$ values compared to those of the other sensors in the same structure (see Fig. 1). This differential behavior can enable the identification of lesions in the breast tissue.

This working principle of the tactile system can be better visualized in Fig. 1 where a right shift of $\lambda_B$ occurs in the FBG (i.e., FBG2) directly located in the body structure under the loaded contact head. It should be noted that each FBG in the body structure has a specific $\lambda_B$ (i.e., $\lambda_B^{FBG1}$, $\lambda_B^{FBG2}$, $\lambda_B^{FBG3}$) value to avoid any overlap in the sensors' responses during the system's functioning. Furthermore, in the application of interest, the impact of $\Delta T$ on the FBGs output is considered negligible, since only the contact heads are designed to push against the tissue while the sensors encapsulated into the body structure are not directly exposed to $T$ changes.

## III. FINITE ELEMENT GUIDED DESIGN OPTIMIZATION AND MANUFACTURING OF THE MULTI-SENSOR TACTILE SYSTEM

### A. Geometry Description

The design of the multi-sensor tactile system is based on the geometry of the single unit originally described in [22], but rescaled by 50% of the original dimensions. This geometry reduction compared to the original design improves the system capability of highly spatial resolving the mapped tissue. The dimensions of the multi-sensor tactile system obtained by the replication of three single units introduced in [22] are shown in Fig. 2. It should be noted that, by changing the width $\delta$ of the intercolumns, the free span under each head can be changed, thus modifying the bending stiffness of the whole structure. Specifically, three body structures (i.e., two-flanges, four-flanges, and six-flanges) characterized by three different values of $\delta$ have been considered in this work, as illustrated in Table I.

The aim of this parametric analysis is to optimize the length of the free span, searching for the configuration where the effects of an external $F$ are easily detectable and interpretable. In all analyzed geometries, the reference coordinate system is $\{C, x, y, z\}$, positioned at the center of the structure with the $x$-axis aligned with the optical fiber direction. Perfect bonding between the optical fiber and the surrounding structure has been assumed so that the displacements and deformations of the two are the same. Under this assumption, it is possible to avoid the representation of the fiber in the finite element model (FEM) as a separate body, which would require very fine mesh discretization and, consequently, very onerous computation times. Fig. 2. also illustrates the location of the individual FBGs, which are long $L_{FBG} = 5$ mm each, and symmetrically centered under each head. The static FEM simulations have been carried out considering three loading cases representing possible resistance reactions of the underlying soft tissue containing a stiffer inclusion (e.g., a tumor): 1) case $3 - 3 - 3$ N, where a $F_y = -3$ N is applied on each contact head (modeling a large inclusion embraced by the whole structure); 2) case $9 - 0 - 0$ N, where a $F_y = -9$ N is applied on one of the lateral heads (modeling an inclusion directly underneath one of these heads); and 3) case $0 - 9 - 0$ N, where a $F_y = -9$ N is applied on the central head (hence, an inclusion right at the center of the array). As kinematic constraints, the bottom faces of the vertical columns are fixed ($u_x = u_y = u_z = 0$) to represent the presence of a support structure not included in the model. Linear elasticity has been assumed, in particular, the body structure has been considered to be made of TPU95A ($E = 26$ MPa, $v = 0.49$), while the heads are in polylactic acid (PLA) ($E = 1$ GPa, $v = 0.3$).

Three models have been built, corresponding to the designs of Table I, and meshed with quadratic elements of maximum side length of $0.02 L_{FBG}$ in the body structure and $0.06 L_{FBG}$ on the contact heads. Each of these models has been loaded with the three considered loading scenarios, for a total of nine simulations.
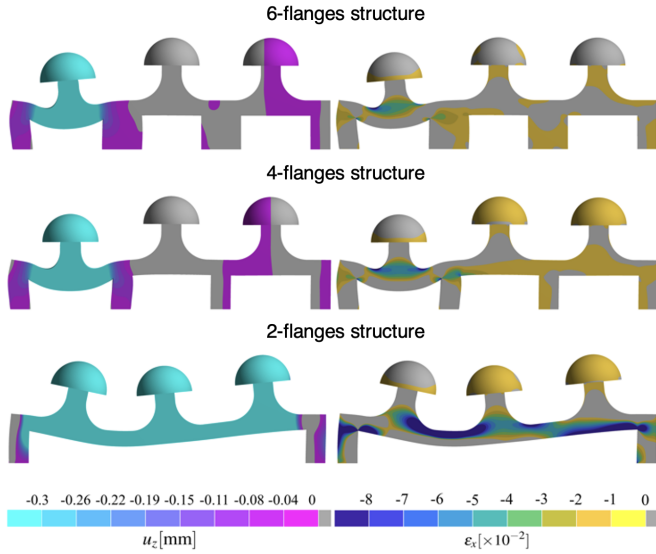
Fig. 3. FEM results for the $9 - 0 - 0$ N case in terms of the vertical displacement (left) and axial strain (right) compared for the analyzed structures. The deformed configuration of the two-flanges case is not in scale with the others.

The simulation results are first illustrated in Fig. 3. in terms of volume plots of the vertical displacement ($u_z$) and the strain along the FBG direction ($\varepsilon_x$) for the loading case $9 - 0 - 0$ N (the other plots have not been included for brevity). On the other hand, Fig. 4. represents the axial strain $\varepsilon_x(x)$ along the fiber location. It should be highlighted that in this loading case, the two-flange structure attains very large displacements ($\simeq -17$ mm) and strains ($\simeq \pm 7\%$ both in traction and compression). Similar results for the two-flange structure are worsened in the other loading cases as well, which makes this specific design impractical for the intended application.

On the other hand, as shown in Fig. 3, the six-flange and four-flange designs have a somewhat similar structural response. However, Fig. 4 shows that the four-flange design exhibits a more stable structural response than the two-flange design for a variation of the loading conditions. This can be proven by considering the loading scenarios where a single $F$ is applied (i.e., $9 - 0 - 0$ N and $0 - 9 - 0$ N), and the FBG segments located under the loaded head (i.e., S1 and S2, respectively). In these cases, the values of $\varepsilon_x(x)$ across S1 and S2 are much more similar in the four-flange structure than the two-flange one. A similar conclusion can be drawn by comparing the $3 - 3 - 3$ N results for the two designs.

A key parameter of the overall structural response of the FBG is the average axial strain $\langle \varepsilon_x \rangle = (1/L_{\text{FBG}}) \int_0^{L_{\text{FBG}}} \varepsilon_x(x) dx$ which indicates whether the detecting portions $L_{\text{FBG}}$ of the fiber are under compression or traction. As shown in Table II, in general, the value of $\langle \varepsilon_x \rangle$ for the FBG directly under the engaged head is positive, while the other FBGs experience negative values. In particular, the two-flanges structure experiences large deformations, confirming the nonviability of this design.

## B. Manufacturing Process

Once the optimal design for the multi-sensor tactile system was identified by FEM, the manufacturing process started.

An array of three FBGs (commercialized by Technica Optical Components, Atlanta, GA, USA) was chosen with the following properties: 5 mm of grating length for each FBG, edge-to-edge spacing of 10 mm, $\lambda_{\text{B}}^{\text{FBG1}}$ of 1530 nm, $\lambda_{\text{B}}^{\text{FBG2}}$ of 1540 nm, $\lambda_{\text{B}}^{\text{FBG3}}$ of 1550 nm, and reflectivity values $>70\%$.

Among various 3-D printing techniques, fused deposition modeling (FDM) was selected to fabricate all the components; thanks to its high repeatability, easy and quick manufacturing process, limited cost, and reduced fabrication time [26], [33].

The manufacturing process starts with the CAD model of the proposed tactile system. In more detail, the 3-D body structure in which the FBG array is intended to be encapsulated, the base for the flanges accommodation, and the contact heads for tissue palpation were designed using the software Onshape. Fig. 5 shows the shape and dimensions of the components of the multi-sensor tactile system to print.

Two materials with different stiffness were chosen for printing the three parts. In more detail, the base and the contact heads were manufactured in PLA, whereas the body structure was printed in TPU 95A to make the sensing element more flexible. In this way, when an $F$ is applied on a contact head, the structure in which the FBG array is encapsulated experiences a flexion leading to a change in the FBG output.

The fabrication was carried out utilizing an FDM printer (i.e., Sovol SV04). The 3-D printing process of the body structure of the tactile system consists of three main steps detailed below (Fig. 6).

*Step 1:* In this phase, slicing software (i.e., Ultimaker CURA) was used to generate the g.code file and to set the printing parameters (i.e., infill density: 100%, infill pattern: triangles, print speed: 30 mm/s, layer height: 0.12 mm).

*Step 2:* The FDM printing process started. The fabrication process involved the layer-by-layer deposition of the molted filament by the nozzle until the grooved channel for the optical fiber integration in the 3-D-printed structure was created. At this stage, the printing process was temporarily stopped. Then, the optical fiber was tensioned using a pair of magnets at the fiber tips and positioned into the channel for a length of 32 mm in a pretensioned state. The FDM process was resumed and the FBG array encapsulated into the body structure.

*Step 3:* Once the printing process was concluded, each component was removed from the printer plate.

As regards the fabrication of the contact heads and the base, a similar process was followed without interrupting the printing process for the FBG encapsulation. A photograph of the final prototype is shown in Fig. 7.

## IV. METROLOGICAL CHARACTERIZATION OF THE MULTI-SENSOR TACTILE SYSTEM

Once the multi-sensor tactile system was manufactured, we proceeded with its metrological characterization.

Considering its application in superficial breast palpation, we focused on investigating the response to $F$ of the system. In addition, we analyzed the crosstalk phenomenon among the three FBGs encapsulated in the body structure.
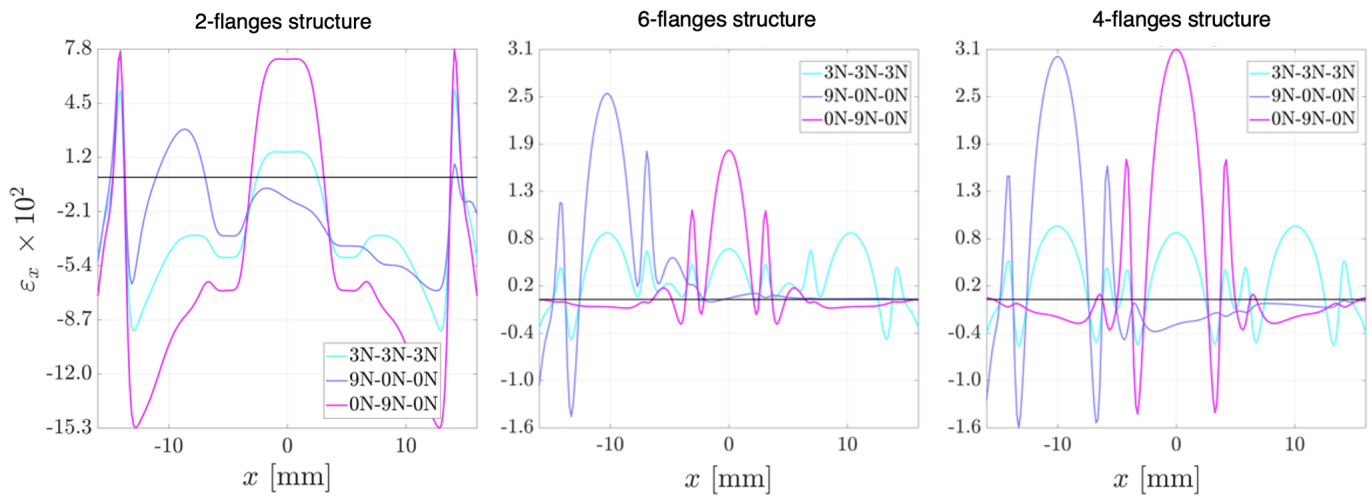
Fig. 4. Effects of loading scenarios on the FBG segment. Axial strain $\varepsilon_x(x)$ for the two-flange, four-flange, and two-flange structures.

TABLE II
AVERAGE AXIAL STRAIN $\langle \varepsilon_x \rangle$ FOR ALL THE ANALYZED CASES

|  | 6-flanges | | | 4-flanges | | | 2-flanges | | |
|---|---|---|---|---|---|---|---|---|---|
|  | A | B | C | A | B | C | A | B | C |
| S1 | 0.54 | 1.70 | -0.09 | 0.64 | 2.2 | -0.22 | -5.2 | 0.97 | -10.7 |
| S2 | 0.35 | 0.02 | 0.99 | 0.56 | -0.32 | 2.3 | 0.13 | -1.3 | 6.6 |
| S3 | 0.54 | 0.01 | -0.09 | 0.64 | -0.07 | -0.22 | -5.3 | -5.8 | -10.7 |

The rows refer to the location of the FBG element S1, S2, S3, while the columns refer to the loading scenario: A = 3N-3N-3N, B = 9N-9N-9N, C = 0N-9N-0N.
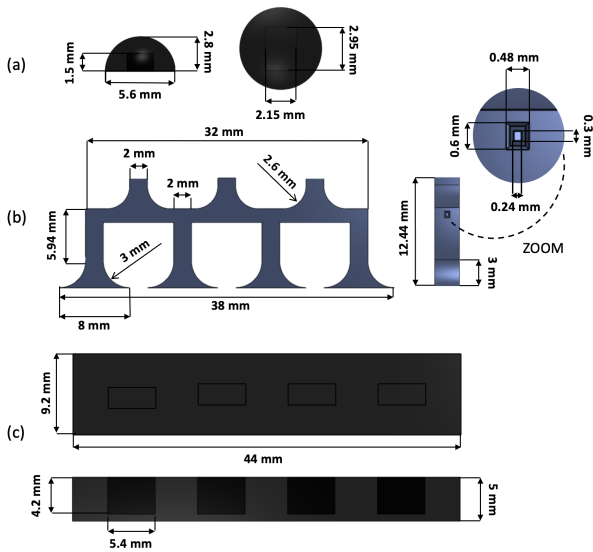


Fig. 5. Design and dimensions of the components of the multi-sensor tactile system (a) contact head, (b) body structure with a focus on the grooved channel for the encapsulation of the FBG array during the FDM process, and (c) base.

## A. Response to Force: Experimental Setup, Data Analysis, and Results

The experimental protocol employed for the metrological characterization of the FBG array integrated into the body structure of the tactile system falls into three different case studies. In more detail, the sensitivity to $F$ ($S_F$) of FBG1 and the crosstalk effects on FBG2 and FBG3 were analyzed in the Case Study 1, the $S_F$ of FBG2 and the crosstalk effects on FBG1 and FBG3 in Case Study 2, and the $S_F$ of FBG3 and the crosstalk effects on FBG 1 and FBG2 in the Case Study 3.

In each case study, a testing machine (i.e., Instron mod. 3365) was used to evaluate the response to $F$ and the crosstalk phenomenon. In particular, three different 3-D-printed blocks (one for each case study) were fabricated to allow the application of $F$ exclusively on FBG1 in Case Study 1, on FBG2 in Case Study 2, and on FBG3 in Case Study 3.

$F$ values ranging from ∼0 to 9 N were selected to extensively cover force intensities typically applied in a clinical scenario [4]. The tactile system fitting the base was attached to the upper plate of the machine, whereas the 3-D-printed multi-sensor block in PLA was positioned on the bottom plate (see Fig. 8). During the application of $F$, we simultaneously recorded the output of the FBGs in the body structure using an optical interrogator (i.e., si255 Micron Optics) and the $F$ values recorded by the testing machine. All the signals were acquired at a sampling frequency of 100 Hz. A number of ten tests were conducted to investigate the repeatability of the responses and a low displacement rate was set (i.e., 2 mm/min) to ensure quasi-static conditions for each case study.

The recorded data were analyzed in a MATLAB environment to extract the calibration curves ($\Delta\lambda_B$ vs. $F$) for FBG1, FBG2, and FBG3 in the Case Studies 1, 2, and 3, respectively. Each calibration curve was obtained by averaging
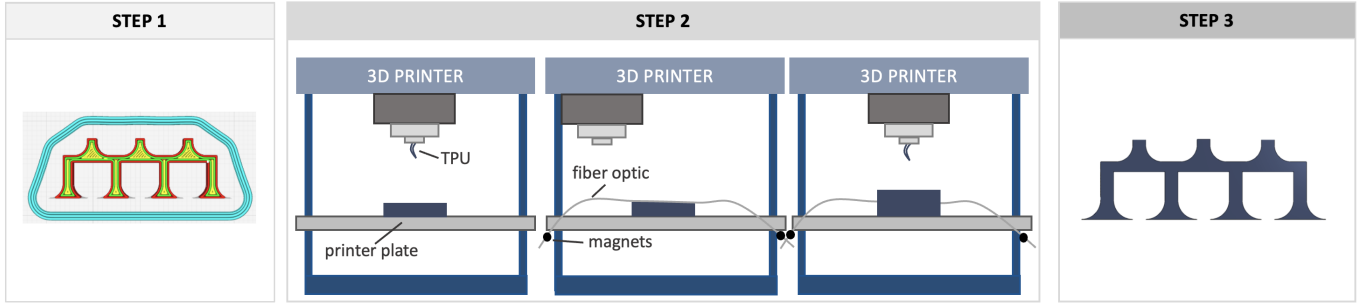
Fig. 6. Representation of the manufacturing steps of the body structure.



Fig. 7. Photograph of the final prototype, including the base, body structure, and contact heads.
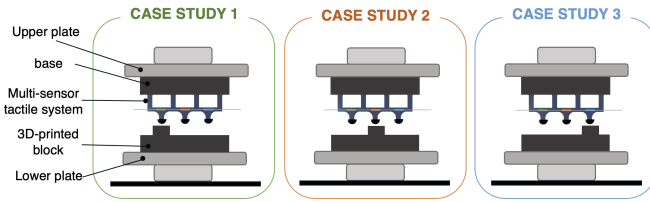


Fig. 8. Scheme of the experimental setup of the three case studies. The multi-sensor tactile system inserted in its base is located on the upper plate of the testing machine, whereas the 3-D-printed structures to apply $F$ on a specific contact head are placed on the lower plate.

TABLE III
CALIBRATION CURVES AND MEAN SENSITIVITY TO $F$ OF THE
MULTI-SENSOR TACTILE SYSTEM

| FBG | Calibration Curve | $S_{F,mean}$ |
|---|---|---|
| FBG 1 | $\Delta\lambda_B = 0.0012 \cdot F^2 + 0.0247 \cdot F$ <br> $R^2 = 0.99$ | 0.037 nm/N |
| FBG 2 | $\Delta\lambda_B = 0.0016 \cdot F^2 + 0.0292 \cdot F$ <br> $R^2 = 0.99$ | 0.044 nm/N |
| FBG 3 | $\Delta\lambda_B = 0.0039 \cdot F^2 + 0.0092 \cdot F$ <br> $R^2 = 0.98$ | 0.046 nm/N |

the FBG output signals in response to the applied $F$ recorded over the ten tests. Then, the interpolation curve that best fits the experimental data recorded by FBG1, FBG2, and FBG3 was computed showing a second-order polynomial trend (see Fig. 9—blue boxes). Table III shows the equations of the fitting curve for each FBG response. The extended uncertainty was also estimated, by using a $t$-Student distribution with a level of confidence of 95% and nine degrees of freedom.

Considering these nonlinear behaviors in Fig. 9, $S_F$ values can be expressed in terms of mean $S_F$ ($S_{F,\text{mean}}$) as follows:

$$S_{F,\text{mean}} = \frac{\Delta\lambda_B\left(F^{\text{max}}\right) - \Delta\lambda_B\left(F^0\right)}{F^{\text{max}} - F^0} \qquad (3)$$

with $\Delta\lambda_B(F^{\text{max}})$ and $\Delta\lambda_B(F^0)$ the value of $\Delta\lambda_B$ at $F^{\text{max}}$ (i.e., 9 N) and $F^0$ (i.e., $\sim$0 N), respectively. We obtained a $S_{F,\text{mean}}^{\text{FBG1}}$ value of 0.037 nm/N, a $S_{F,\text{mean}}^{\text{FBG2}}$ of 0.044 nm/N, and $S_{F,\text{mean}}^{\text{FBG3}}$ of 0.046 nm/N for FBG1, FBG2, and FBG3, respectively.

As expected, an increase in $\Delta\lambda_B$ with $F$ occurs for each sensor, demonstrating the traction of the FBGs within the array encapsulated into the body structure due to shape changes already proposed in [11] and [22].

The slight differences in $S_{F,\text{mean}}$ values among the three sensors are presumably related to difficulties in guaranteeing the same pre-tensioning for all the FBGs integrated into the structure.

### B. Crosstalk Effect: Data Analysis and Results

In each case study, we also investigated the crosstalk phenomenon on the two other unloaded sensors within the body structure. As for the calibration curve, an average of the response of these two sensors was computed over the ten tests showing a not negligible crosstalk effect (see Fig. 9).

Specifically, when an $F$ is applied to FBG1, both FBG2 and FBG3 experience an output variation with an amplitude approximately more than half of the one of FBG1 [maximum output of 0.13 nm for FBG2 and 0.06 nm for FBG3 compared to 0.33 nm for FBG1 as reported in Fig. 9(a)]. A similar result is observed for FBG1 and FBG3 when FBG2 is the loaded sensor [maximum output of 0.16 nm for FBG1 and 0.20 nm for FBG3 compared to 0.39 nm for FBG2 as reported in Fig. 9(b)] and for FBG1 and FBG2 when FBG3 is loaded [maximum output of 0.13 nm for FBG1 and 0.20 nm for FBG2 compared to 0.41 nm for FBG3 as reported in Fig. 9(c)].

For each case study, we evaluate the crosstalk coefficient (CS) to decouple the effect of the loaded sensor from the output of the two other unloaded sensors integrated into the same 3-D-printed structure

$$\text{CS}_{\text{loaded sensor}}^{\text{unloaded sensor}} = \frac{\Delta\lambda_{B\,\text{unloaded sensor}}^{\text{max}}}{\Delta\lambda_{B\,\text{loaded sensor}}^{\text{max}}} \qquad (4)$$

where $\Delta\lambda_{B\,\text{unloaded sensor}}^{\text{max}}$ represents the maximum output change of the unloaded sensor (FBG2 and FBG3 in the Case Study 1, FBG1 and FBG3 in the Case Study 2, and FBG1 and FBG2 in the Case Study 3), while $\Delta\lambda_{B\,\text{loaded sensor}}^{\text{max}}$ the maximum output change of the loaded sensor (FBG1 in the Case Study 1, FBG2 in the Case Study 2, and FBG3 in the Case Study 3). Therefore, we obtained a $\text{CS}_{\text{FBG1}}^{\text{FBG2}}$ of
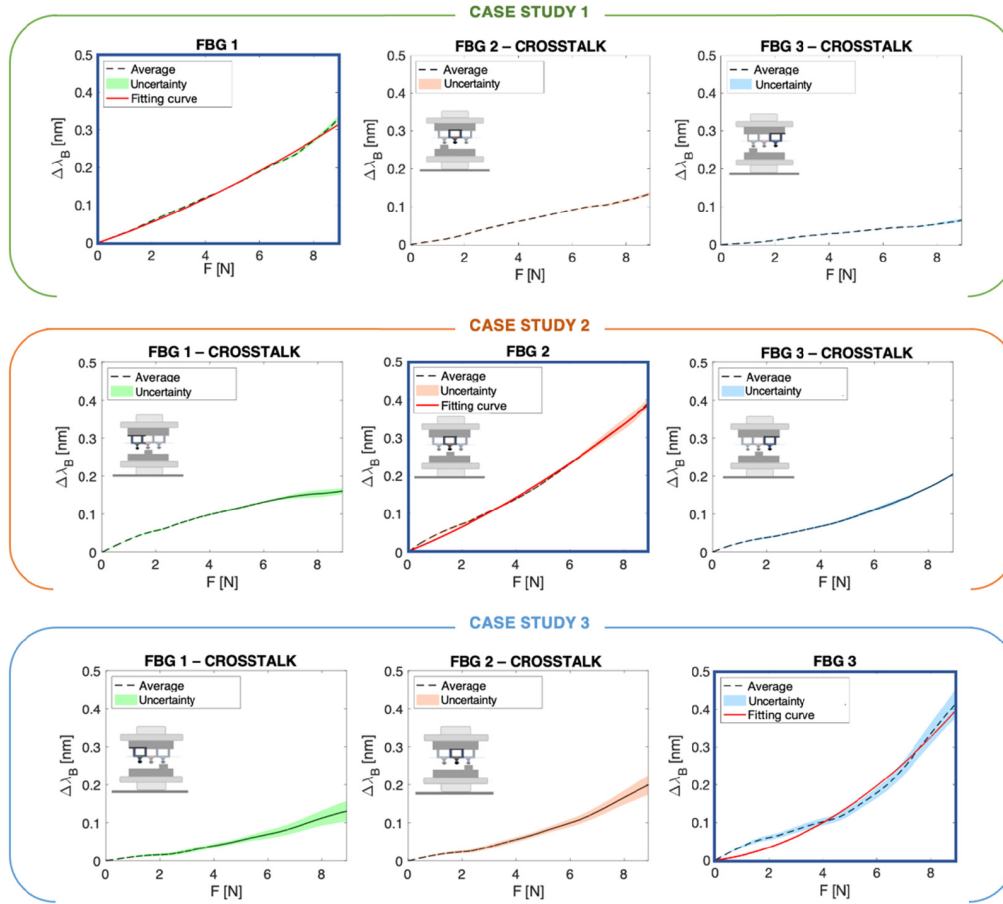
Fig. 9. Results of the three case studies. Specifically, for each one, the mean response $\Delta\lambda_B$ versus $F$ (black line), the expanded uncertainty (shaded area), and the fitting curve of the loaded FBG are reported and highlighted with a blue box. In addition, the mean response $\Delta\lambda_B$ versus $F$ (black line) and the expanded uncertainty (shaded area) of the other two unloaded FBGs, which represent the crosstalk phenomena, are shown.

0.015 nm/N and a $CS_{FBG1}^{FBG3}$ of 0.007 nm/N in Case Study 1, a $CS_{FBG2}^{FBG1}$ value of 0.018 nm/N and a $CS_{FBG2}^{FBG3}$ of 0.023 nm/N in Case Study 2, and a $CS_{FBG3}^{FBG1}$ value of 0.015 nm/N and a $CS_{FBG3}^{FBG2}$ of 0.023 nm/N in Case Study 3.

## V. TESTS ON PHANTOMS MIMICKING BREAST TISSUE WITH A TUMOR

In this section, we investigated the ability of the developed multi-sensor tactile system to detect the presence of a harder material (i.e., a block of PLA) inside an ultra-stretchable silicone sample. To investigate the capability of each FBG, we fabricated three phantoms with the PLA block at the same depth ($z$-axis) but localized at three different positions in the $xy$ plane.

### A. Fabrication Process of the Phantoms

Each phantom is made of an ultra-stretchable silicone material (i.e., Eco-Flex Gel 2) that mimics the soft tissue of the breast and a PLA block embedded inside the silicone to simulate the presence of a tumor. Each phantom was fabricated to test the ability of one of the three FBGs embedded into the body structure to detect materials with different stiffness. Since three FBGs were encapsulated into the body structure, three different phantoms were developed. In each phantom, the reference coordinate system is $\{C, x, y, z\}$, positioned at

the center of the top face of the silicone as shown in Fig. 10. Each phantom integrates the PLA block at a depth ($z$-axis) of 5 mm to simulate the presence of a superficial tumor in the breast tissue. However, the position of the PLA block in the $xy$ plane varies in the three phantoms so that the center of each block is directly underneath the center of the FBG under investigation.

The design and fabrication process of each phantom involves the following stages (see Fig. 10).

1) A parallelepiped-shaped mold with dimensions $50 \times 50 \times 20$ mm was fabricated in PLA by using an FDM printer (i.e., Sovol SV04). The mold has an open-top surface to promote the pouring of the polymer inside. Subsequently, a block with dimensions $8 \times 8 \times 14$ mm was fabricated in PLA for mimicking a tumor mass.

2) Four holes were made on the lateral faces of the PLA block and mold. The holes on the lateral faces of the mold were drilled at the center of each face, as shown in the front view in Fig. 10. As for the PLA block, the holes were made on each side face at a depth of 5 mm from the top face (see Fig. 10). Then, two cotton wires were inserted through the holes to guarantee the proper positioning of the tumor inside the silicone. Finally, the wires were tensioned and attached to the lateral faces of the mold using adhesive tape. In this way, we ensure that
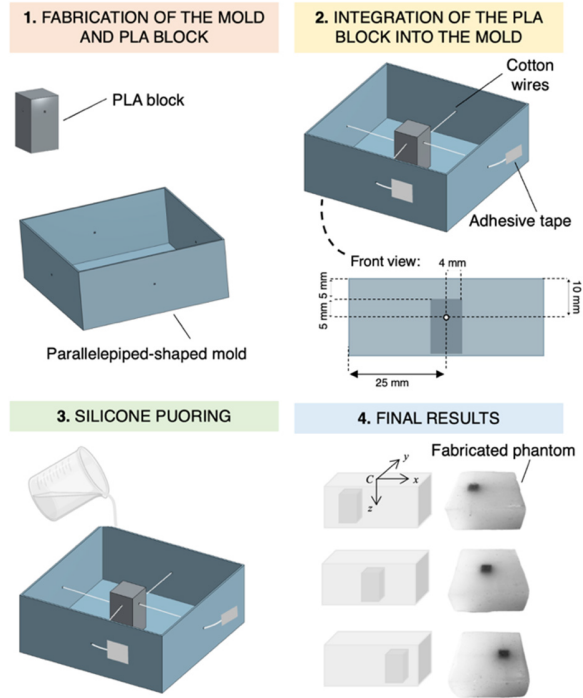
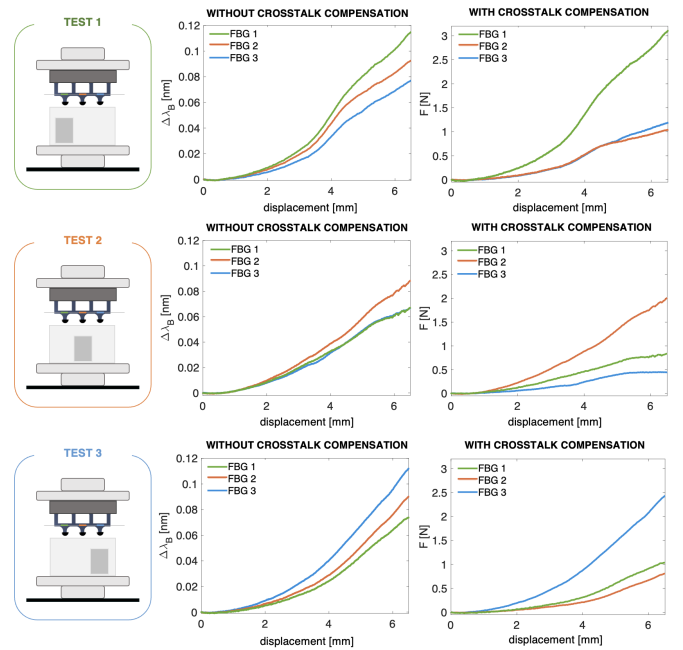Fig. 10.  Stages of the fabrication process of phantoms and photographs of the three fabricated phantoms.



Fig. 11.  Experimental set-up and results of the three palpation tests, one for each of the three phantoms. The results of each test in terms of $\Delta\lambda_B$ versus displacement without crosstalk compensation and $F$ versus displacement with crosstalk compensation are shown.

the block integrated into the silicone at the chosen depth remains in place during polymer pouring, preventing any possible translation or rotation.

3) The silicone rubber preparation and pouring process was carried out. The silicone was prepared following the producer's instructions and poured into the parallelepiped-shaped mold. After a curing time of 50 min, the phantom with the embedded PLA block was ready to be removed from the mold.

### B. Palpation Tests on Phantoms: Experimental Setup, Data Analysis, and Results

The ability to discriminate the presence of a tumor mass inside the breast tissue was investigated by carrying out three palpation tests, one for each of the three phantoms to simulate the scenario in which a single contact head encounters a rigid mass inside the tissue. In particular, Test 1 investigated the ability of FBG1 to identify a stiffer mass within the silicone, Test 2 of FBG2, and Test 3 of FBG3.

We performed compression tests with the same testing machine used for the metrological characterization to apply a controlled displacement along the $z$-axis from ∼0 to 6.5 mm. The multi-sensor tactile system was stuck on the upper plate of the machine, whereas each phantom was placed on the lower plate to simulate the functioning of the sensing structure in a real scenario. During these tests, we simultaneously recorded the output of the three FBGs integrated into the same structure by using the optical interrogator and the value of the displacement from the testing machine. All the signals were acquired at a sampling frequency of 100 Hz.

Data were analyzed in MATLAB environment by taking into account the $S_F$ values in Section IV-A and the effect of crosstalk analyzed in Section IV-B. Then, results are reported in terms of $F$ versus displacement. In more detail, we compen-

sated the crosstalk effect from the raw data of the sensors not directly affected by the presence of the PLA block as shown below

$$\Delta\lambda_{B\,\text{unloaded sensor}}^{\text{final}} = \Delta\lambda_{B\,\text{unloaded sensor}}^{\text{raw data}} - \Delta\lambda_{B\,\text{loaded sensor}}^{\text{raw data}} \cdot \text{CS}_{\text{loaded sensor}}^{\text{unloaded sensor}} \quad (5)$$

where $\Delta\lambda_{B\,\text{unloaded sensor}}^{\text{raw data}}$ and $\Delta\lambda_{B\,\text{unloaded sensor}}^{\text{final}}$ represent the raw output and final output after crosstalk compensation of the FBG not directly affected by the presence of the stiffer mass (i.e., FBG2 and FBG3 in Test 1, FBG1 and FBG3 in Test 2, and FBG1 and FBG2 in Test 3), respectively, while $\Delta\lambda_{B\,\text{loaded sensor}}^{\text{raw data}}$, the raw output of the FBG that encounters the rigid block during the compression test.

The results of the three palpation tests are shown in Fig. 11. Specifically, in Fig. 11 (left column) for each compression test, the $\Delta\lambda_B$ versus displacement trends without the crosstalk compensation (i.e., $\Delta\lambda_{B\,\text{loaded FBG1}}^{\text{raw data}}$, $\Delta\lambda_{B\,\text{unloaded FB2}}^{\text{raw data}}$, and $\Delta\lambda_{B\,\text{unloaded FB3}}^{\text{raw data}}$ for Test 1, $\Delta\lambda_{B\,\text{loaded FBG2}}^{\text{raw data}}$, $\Delta\lambda_{B\,\text{unloaded FB1}}^{\text{raw data}}$, and $\Delta\lambda_{B\,\text{unloaded FB3}}^{\text{raw data}}$ for Test 2, $\Delta\lambda_{B\,\text{loaded FBG3}}^{\text{raw data}}$, $\Delta\lambda_{B\,\text{unloaded FB1}}^{\text{raw data}}$, and $\Delta\lambda_{B\,\text{unloaded FB2}}^{\text{raw data}}$ for Test 3) are reported. Then, Fig. 11 (right column) shows for the three tests the output signals in which the crosstalk phenomena were compensated and the $\Delta\lambda_B$ output trends were reported in terms of $F$ using the values of $S_F$.

From the achieved results without crosstalk compensation (left column of Fig. 11), the identification of which FBGs in each test encountered a hard inclusion inside the soft material could be potentially carried out. It seems possible considering that in each test greater values of $\Delta\lambda_B$ are registered by the FBG pressed against a stiffer mass. However, when crosstalk compensation is applied, the differential behavior of the three FBGs should be emphasized and the identification of hard

inclusions facilitated. Indeed, from the signals with crosstalk compensation (right column of Fig. 11), the $F$ values recorded by the FBG that encounters the stiffer mass in each test are more than three times higher than those of the sensors not involved in tumor identification (i.e., maximum $F$ value of 1.04 N for FBG2 and 1.18 N for FBG3 compared to 3.10 N for FBG1 in Test 1, maximum $F$ value of 0.83 N for FBG1 and 0.44 N for FBG3 compared to 2.01 N for FBG2 in Test 2, and maximum $F$ value of 1.03 N for FBG1 and 1.81 N for FBG2 compared to 2.43 N for FBG3 in Test 3). Moreover, results showed that the sensors not directly affected by the presence of the block reached a value of $F$ always lower than $\sim$1 N making easier the identification of a tumor within a tissue.

## VI. Discussion and Conclusion

In this article, we proposed a multi-sensor tactile system to discriminate materials with varying stiffness for the timely identification of breast tumors. It represents an optimization of a previously developed prototype presented in [11] and [22], that was based on a single FBG. The two key achievements are: 1) a reduction in dimensions of the sensing structure by 50% and 2) a multi-sensor approach (from a single FBG to three FBGs integrated into the same structure). Specifically, an array of three FBGs was used as a first step toward the creation of a 3 × 3 matrix of sensors for superficial breast tissue palpation. These improvements increase the spatial resolution of the tactile system and enable the simultaneous investigation of multiple measurement sites.

Compared to existing solutions that incorporate multiple sensing units separately [11], [15], [16], our multi-sensor tactile system represents the first solution that exploits the multiplexing property of FBGs to embed only one optical fiber with three FBGs into the same 3-D-printed structure. This approach enables the minimization of the encumbrance of the probe, improves its spatial resolution, and shows the great advantage of reducing the connections to the optical interrogator to acquire the output signals.

An FEM was conducted to determine the appropriate shape and FBGs positioning within the tactile system, ensuring a good tradeoff between flexibility and robustness. Then, the FDM method was chosen for manufacturing each component of the system. Subsequently, the metrological properties of the proposed structure were investigated in terms of $S_F$ and crosstalk effects. In particular, as regards the sensors response to $F$, an $S_{F,\text{mean}}^{\text{FBG1}}$ value of 0.037 nm/N, an $S_{F,\text{mean}}^{\text{FBG2}}$ of 0.044 nm/N, and an $S_{F,\text{mean}}^{\text{FBG3}}$ of 0.046 nm/N were obtained for FBG1, FBG2, and FBG3, respectively.

Furthermore, palpation tests were carried out on phantoms mimicking breast tissue with lesions. By taking into account the compensation of the crosstalk among sensors in the same 3-D-printed structure, the results, although preliminary, demonstrated the ability of the multi-sensor tactile system to discriminate superficial hard lesions within a healthy soft tissue. This capability can lead to an immediate recognition of the presence of a lesion and its position in the palped tissue.

Future developments will be first devoted to further increasing the number of FBGs integrated into the body structure to create a 3 × 3 matrix of sensors for noninvasive tissue palpa-

tion. Moreover, the proposed FEM will be optimized to model the fiber-polymer interfacial interactions. Then, the promising results in the present work will foster the development of artificial intelligence techniques to automatically detect breast tumor masses from the experimental data acquired by the proposed system. Furthermore, future validation will involve not only phantoms mimicking breast tissue with tumors, but also patients, expanding the applicability of the device in real-world application scenarios. In these settings, potential feedback may be provided to the user (patient or clinicians) to report specific threshold exceedances making the proposed multi-sensor tactile a useful tool for supporting the medical practice during diagnostic palpation examinations.

## References

[1] M. M. Koo, C. von Wagner, G. A. Abel, S. McPhail, G. P. Rubin, and G. Lyratzopoulos, "Typical and atypical presenting symptoms of breast cancer and their associations with diagnostic intervals: Evidence from a National Audit of Cancer diagnosis," *Cancer Epidemiol.*, vol. 48, pp. 140–146, Jun. 2017, doi: 10.1016/j.canep.2017.04.010.

[2] C.-H. Won, J.-H. Lee, and F. Saleheen, "Tactile sensing systems for tumor characterization: A review," *IEEE Sensors J.*, vol. 21, no. 11, pp. 12578–12588, Jun. 2021, doi: 10.1109/JSEN.2021.3078369.

[3] P. Puangmali, K. Althoefer, L. D. Seneviratne, D. Murphy, and P. Dasgupta, "State-of-the-art in force and tactile sensing for minimally invasive surgery," *IEEE Sensors J.*, vol. 8, no. 4, pp. 371–381, Apr. 2008, doi: 10.1109/JSEN.2008.917481.

[4] J. Konstantinova, M. Li, G. Mehra, P. Dasgupta, K. Althoefer, and T. Nanayakkara, "Behavioral characteristics of manual palpation to localize hard nodules in soft tissues," *IEEE Trans. Biomed. Eng.*, vol. 61, no. 6, pp. 1651–1659, Jun. 2014.

[5] J. G. Elmore, K. Armstrong, C. D. Lehman, and S. W. Fletcher, "Clinician's corner screening for breast cancer," *J. Amer. Med. Assoc.*, vol. 293, no. 10, pp. 1245–1256, 2005.

[6] H. Madjar, H. A. Ladner, W. Sauerbrei, A. Oberstein, H. Prömpeler, and A. Pfleiderer, "Preoperative staging of breast cancer by palpation, mammography and high-resolution ultrasound," *Ultrasound Obstetrics Gynecol.*, vol. 3, no. 3, pp. 185–190, 1993, doi: 10.1046/j.1469-0705.1993.03030185.x.

[7] W. Alomaim, D. O'Leary, J. Ryan, L. Rainford, M. Evanoff, and S. Foley, "Subjective versus quantitative methods of assessing breast density," *Diagnostics*, vol. 10, no. 5, p. 331, May 2020, doi: 10.3390/diagnostics10050331.

[8] N.-J. Park, D.-H. Kang, and M. T. Weaver, "Objective and subjective breast cancer risk: Relationships with natural killer cell activity and psychological distress in healthy women," *Cancer Nursing*, vol. 33, no. 6, pp. 411–420, Nov. 2010, doi: 10.1097/NCC.0b013e3181dc37a1.

[9] D. Saslow et al., "Clinical breast examination: Practical recommendations for optimizing performance and reporting," *CA, Cancer J. Clinicians*, vol. 54, no. 6, pp. 327–344, Nov. 2004, doi: 10.3322/canjclin.54.6.327.

[10] J. C. Gwilliam, Z. Pezzementi, E. Jantho, A. M. Okamura, and S. Hsiao, "Human vs. robotic tactile sensing: Detecting lumps in soft tissue," in *Proc. IEEE Haptics Symp.*, Mar. 2010, pp. 21–28, doi: 10.1109/HAPTIC.2010.5444685.

[11] D. Lo Presti et al., "A 3-D-printed tactile probe based on fiber Bragg grating sensors for noninvasive breast cancer identification," *IEEE Sensors J.*, vol. 23, no. 20, pp. 24489–24499, Oct. 2023, doi: 10.1109/JSEN.2023.3306970.

[12] Y. Murayama et al., "Development of a new instrument for examination of stiffness in the breast using haptic sensor technology," *Sens. Actuators A, Phys.*, vol. 143, no. 2, pp. 430–438, May 2008, doi: 10.1016/j.sna.2007.11.035.

[13] V. Egorov and A. P. Sarvazyan, "Mechanical imaging of the breast," *IEEE Trans. Med. Imag.*, vol. 27, no. 9, pp. 1275–1287, Sep. 2008, doi: 10.1109/TMI.2008.922192.

[14] W. Du et al., "Conformable ultrasound breast patch for deep tissue scanning and imaging," *Sci. Adv.*, vol. 9, no. 30, pp. 1–13, 2023, doi: 10.1126/sciadv.adh5325.

[15] T. Li, C. Shi, and H. Ren, "A high-sensitivity tactile sensor array based on fiber Bragg grating sensing for tissue palpation in minimally invasive surgery," *IEEE/ASME Trans. Mechatronics*, vol. 23, no. 5, pp. 2306–2315, Oct. 2018, doi: 10.1109/TMECH.2018.2856897.

[16] R. Hampson, G. West, and G. Dobie, "Tactile, orientation, and optical sensor fusion for tactile breast image mosaicking," *IEEE Sensors J.*, vol. 23, no. 5, pp. 5315–5324, Mar. 2023, doi: 10.1109/JSEN.2023.3237906.

[17] C. Lv, S. Wang, and C. Shi, "A high-precision and miniature fiber Bragg grating-based force sensor for tissue palpation during minimally invasive surgery," *Ann. Biomed. Eng.*, vol. 48, no. 2, pp. 669–681, Feb. 2020, doi: 10.1007/s10439-019-02388-w.

[18] J. Li, C. Wang, Z. Mao, Y. Liu, Z. Wang, and H. Liu, "A compact FBG-based triaxial force sensor with parallel helical beams for robotic-assisted surgery," *IEEE Trans. Instrum. Meas.*, vol. 71, pp. 1–9, 2022, doi: 10.1109/TIM.2022.3183672.

[19] A. Abushagur, N. Arsad, M. Reaz, and A. Bakar, "Advances in bio-tactile sensors for minimally invasive surgery using the fibre Bragg grating force sensor technique: A survey," *Sensors*, vol. 14, no. 4, pp. 6633–6665, Apr. 2014, doi: 10.3390/s140406633.

[20] A. Othonos, K. Kalli, and G. E. Kohnke, "Fiber Bragg gratings: Fundamentals and applications in telecommunications and sensing," *Phys. Today*, vol. 53, no. 5, pp. 61–62, May 2000, doi: 10.1063/1.883086.

[21] D. Lo Presti et al., "Fiber Bragg gratings for medical applications and future challenges: A review," *IEEE Access*, vol. 8, pp. 156863–156888, 2020, doi: 10.1109/ACCESS.2020.3019138.

[22] D. Lo Presti et al., "Design optimization and characterization of a 3-D-printed tactile sensor for tissue palpation," *IEEE Sensors J.*, vol. 24, no. 8, pp. 12366–12373, Apr. 2024, doi: 10.1109/JSEN.2024.3369337.

[23] T. Erdogan, "Fiber grating spectra," *J. Lightw. Technol.*, vol. 15, no. 8, pp. 1277–1294, Aug. 1997.

[24] D. Lo Presti, C. Massaroni, and E. Schena, "Optical fiber gratings for humidity measurements: A review," *IEEE Sensors J.*, vol. 18, no. 22, pp. 9065–9074, Nov. 2018, doi: 10.1109/JSEN.2018.2870585.

[25] A. Leal-Junior et al., "Fiber Bragg gratings in CYTOP fibers embedded in a 3D-printed flexible support for assessment of human–robot interaction forces," *Materials*, vol. 11, no. 11, p. 2305, Nov. 2018, doi: 10.3390/ma11112305.

[26] M. Fernandez-Vicente, W. Calle, S. Ferrandiz, and A. Conejero, "Effect of infill parameters on tensile mechanical behavior in desktop 3D printing," *3D Printing Additive Manuf.*, vol. 3, no. 3, pp. 183–192, Sep. 2016, doi: 10.1089/3dp.2015.0036.

[27] H. Wang et al., "SleepSense: Smart pillow with pressure-sensitive FBG-embedded silicone buttons," *IEEE Sensors J.*, vol. 23, no. 17, pp. 19324–19331, Sep. 2023, doi: 10.1109/JSEN.2023.3295114.

[28] H. Wang et al., "Double-fishtail-shaped FBG wearable device for sitting posture recognition and real-time respiratory monitoring," *IEEE Sensors J.*, vol. 24, no. 7, pp. 10164–10171, Apr. 2024, doi: 10.1109/JSEN.2024.3367622.

[29] D. Lo Presti et al., "Plant wearable sensors based on FBG technology for growth and microclimate monitoring," *Sensors*, vol. 21, no. 19, p. 6327, Sep. 2021, doi: 10.3390/s21196327.

[30] D. Lo Presti, D. Bianchi, C. Massaroni, A. Gizzi, and E. Schena, "A soft and skin-interfaced smart patch based on fiber optics for cardiorespiratory monitoring," *Biosensors*, vol. 12, no. 6, p. 363, May 2022, doi: 10.3390/bios12060363.

[31] F. De Tommasi, C. Massaroni, M. A. Caponero, M. Carassiti, E. Schena, and D. L. Presti, "FBG-based mattress for heart rate monitoring in different breathing conditions," *IEEE Sensors J.*, vol. 23, no. 13, pp. 14114–14122, Jul. 2023, doi: 10.1109/JSEN.2023.3275323.

[32] C. Massaroni, M. Caponero, R. D'Amato, D. Lo Presti, and E. Schena, "Fiber Bragg grating measuring system for simultaneous monitoring of temperature and humidity in mechanical ventilation," *Sensors*, vol. 17, no. 4, p. 749, Apr. 2017, doi: 10.3390/s17040749.

[33] D. L. Presti et al., "The effect of infill pattern and density on the response of 3-D-printed sensors based on FBG technology," *IEEE Sensors J.*, vol. 22, no. 20, pp. 19357–19365, Oct. 2022, doi: 10.1109/JSEN.2022.3202101.

**L. Zoboli** received the Ph.D. degree from the Università degli Studi di Roma, Rome, Italy, in 2022.

He is a Postdoctoral Researcher of solid and structural mechanics with the Università Campus Bio-Medico di Roma, Rome. He is currently investigating nonlinear coupled phenomena during the curing phase of polymers. His research activity focuses on polymer modeling, multiscale mechanics, coupled physics, nuclear fusion, and finite-element analysis.

Dr. Zoboli is a member of Associazione Italiana di Meccanica Teorica ed Applicata (AIMETA) and Indam-Gruppo Nazionale per la Fisica Matematica (GNFM).

**F. De Tommasi** (Graduate Student Member, IEEE) received the M.Sc. degree from the Università Campus Bio-Medico di Roma (UCBM), Rome, Italy, in 2020.

She is currently a Postdoctoral Research Fellow with the Unit of Measurements and Biomedical Instrumentation, UCBM. Her research interests focus on the development of FBG-based measurement systems for patient safety enhancement and physiological monitoring.

**C. Massaroni** (Senior Member, IEEE) received the Ph.D. degree from the Università Campus Bio-Medico di Roma (UCBM), Rome, Italy, in 2017.

He is an Assistant Professor with the Unit of Measurements and Biomedical Instrumentation, UCBM. His research interests include the design, development, and testing of wearable devices and unobtrusive measuring systems for medical applications.

**V. Altomare** is a Full Professor of general surgery with the Università Campus Bio-Medico di Roma, Rome, Italy. He is the Director of the Breast Surgical Unit with Fondazione Policlinico Universitario Campus Bio-Medico, Rome. His main research interests include breast cancer management and oncoplastic surgical treatment.

**A. Grasso** received the Ph.D. degree from Fondazione Policlinico Universitario Campus Bio-Medico, Rome, Italy, in 2019.

She is a Consultant Breast Surgeon with the Fondazione Policlinico Universitario Campus Bio-Medico. Her main field of interest is prevention, diagnosis, and treatment of breast diseases. Her research interests include oncoplastic surgery and targeted surgical therapies.

**A. Gizzi** (Senior Member, IEEE) received the Ph.D. degree from the Università Campus Bio-Medico di Roma (UCBM), Rome, Italy, in 2012.

He is an Associate Professor of solid and structural mechanics with UCBM. His main research interests include theoretical and computational biomechanics and mechanobiology.

Dr. Gizzi has been a member of the Executive Board of the European Society of Biomechanics—Italy Chapter and IEEE-Engineering in Medicine and Biology Society (EMBS) since 2023.

**E. Schena** (Senior Member, IEEE) received the Ph.D. degree from Università Campus Bio-Medico di Roma (UCBM), Rome, Italy, in 2007.

He is a Full Professor of measurements with UCBM. His research interests include the design and assessment of wearable.

Dr. Schena became the Chair of the Italy Chapter of the IEEE Sensors Council in 2018.

**M. Pulcinelli** (Graduate Student Member, IEEE) received the M.Sc. (Hons.) degree from the Università Campus Bio-Medico di Roma, Rome, Italy, in 2023, where she is currently pursuing the Ph.D. degree with the Unit of Measurements and Biomedical Instrumentation.

Her research interests include the development of fiber optic-based systems and the application of machine learning algorithms for biomedical applications.

**D. Lo Presti** (Member, IEEE) received the Ph.D. degree from the Università Campus Bio-Medico di Roma (UCBM), Rome, Italy, in 2021.

She is currently an Assistant Professor with the Unit of Measurements and Biomedical Instrumentation, UCBM. Her main research activities focus on the design, fabrication, and feasibility assessment of smart systems and wearables based on fiber optics for biomedical applications.